A Two Layer Electrode Structure for Improved Li Ion Diffusion and Volumetric Capacity in Li Ion Batteries

Chun Huang[a], Neil P. Young[a], Jin Zhang[b], Henry J. Snaith[b], Patrick S. Grant[a]*

[a] Department of Materials, University of Oxford, Parks Road, Oxford, OX1 3PH, UK

[b] Clarendon Laboratory, Department of Physics, University of Oxford, Parks Road, Oxford, OX1 3PH, UK

E-mail: ann.huang@materials.ox.ac.uk

Highlights

• A two layer negative electrode with a different nanomaterial morphology in each layer was first fabricated by a scalable suspension atomization and spray deposition processing technique for Li ion batteries.

• The two layer electrode was designed to contain TiO_2 nanoparticles in one layer and porous TiO_2 particles in the other layer to improve Li ion diffusion dynamics through the electrode thickness.

• The two layer electrode showed a combination of high volumetric capacity and rate capability that was superior to conventional, randomly blended electrodes comprising the same nanomaterials at the same charge/discharge rates.

• The two layer electrode demonstrated a scalable approach to structuring electrodes that can improve energy storage performance and increase active nanomaterial utilization.

Abstract

Nanomaterials with different morphologies were placed in discrete layers through the thickness of a negative electrode for a Li ion battery to exploit effectively the intrinsic energy storage capabilities of each nanomaterial morphology and to improve the overall dynamics of Li ion diffusion. The two layer electrode showed a combination of high volumetric capacity and rate capability that surpassed the performance of conventional randomly blended electrodes comprising the same nanomaterials. Local Li ion concentrations were measured through the electrode thickness and clearly showed the benefits of the layered structure over the alternatives. The two layer electrode was fabricated by a flexible and scalable suspension atomization and spray deposition technique with generic potential for improved layered electrodes in a wide range of applications.

Keywords: lithium ion battery; layer-by-layer; layered electrode; spray processing; porous TiO_2

1 Introduction

Electrical energy storage from renewable sources and for electric vehicles (EVs) can play an important role in meeting growing energy demands and the need to decarbonize the environment. Li ion batteries (LIBs) are used in these applications due to their high energy density of 110-220 Wh kg^{-1} compared with 12-20 Wh kg^{-1} for supercapacitors [1–3]. However, LIBs suffer from a relatively low power density of 0.2-3 kW kg^{-1} compared with 2-10 kW kg^{-1} for supercapacitors [4], which restricts LIB penetration into EVs and large-scale stationary power storage [5]. One of the LIB power constraints is due to restricted Li ion diffusion through the electrodes so that Li ion concentrations tend to be highest close to the separator immersed in a liquid electrolyte, and lowest further from the separator and adjacent

to the current collector, especially under high charge/discharge rates [6], as recently shown by nuclear reaction ion beam analysis [7]. The depletion of Li ions towards the current collector leads to an inhibited contribution to energy capacity from the active material in this region, and reduced power performance [8].

Both experimental and computational studies have demonstrated that the microstructure of LIB electrodes influences key performance metrics [9–12]. For example, investigations of the relationship between electrode particle shape, pore tortuosity and overall porosity showed that increased tortuosity in the plane perpendicular to the current collector decreased power [9]. Investigations of the relationship between porosity, electronic and ionic conductivities also showed that capacity can be optimized by adjusting active and non-active (e.g. electrical conductivity additive) material fractions in electrodes [10]. Although modelling has suggested structuring of electrodes can be beneficial for dynamic response, limited options for manufacturing electrodes has restricted efforts to obtain compelling experimental evidence. For example, all the electrodes in the previous studies mentioned above comprised random, blended arrangements of active and non-active materials, and no consideration was given to optimize ion diffusion dynamics through the electrode thickness [10,13,14], primarily because conventional electrode fabrication techniques cannot realize intentionally heterogeneous electrode structures where different porosity or material fractions are contrived or placed at different locations [9].

Titanium oxide-based materials (anatase TiO_2, TiO_2(B), $Li_4Ti_5O_{12}$, etc.) are promising candidates for fast rechargeable LIB negative electrodes. TiO_2-based electrodes exhibit a relatively low volume expansion upon lithiation of $<$3% [15,16]. Nanostructured TiO_2 with $<$10 nm particle size is potentially attractive for high capacities [17], e.g. TiO_2 with an ordered 3D pore structure (6.5 nm thin walls) exhibited capacities of 240, 175 and 125 mAh g^{-1} at 0.5, 4.5 and 35.7 C, respectively [18].

TiO_2(B) nanoparticulate ($\sim$2 x 4 nm) exhibited capacities of 322 and 200 mAh g^{-1} at 0.1 and 4 C, respectively [19]. Si microtube scaffolds decorated with anatase TiO_2 exhibited a capacity of 150 μAh cm^{-2} at 0.25 C [20]. The otherwise generally poor electrical conductivity of TiO_2 was increased by 61% through coating TiO_2 with carbon [21] and the reversible capacity was increased from 64 to 162 mAh g^{-1} at 6 C through coating TiO_{2-x} nanotubes with carbon and thermal annealing in H_2 [22].

However, all these nanostructured electrodes were intended to have a uniform structure through electrode thickness with a low loading density and therefore had a relatively low volumetric capacity [18]. High volumetric capacities are increasingly recognized as an important parameter for consumer electronics and EV applications [23, 24]. Most electrode manufacturing routes involving nanomaterials also often suffer from a lack of scalability or high cost. The primary objective of this work is not necessarily to obtain the highest reported capacity of TiO_2-based electrodes at different charge/discharge C rates, but to investigate the possible generic benefits on charge storage behavior of arranging different morphologies of nanomaterials in specific locations of an electrode with a particular emphasis on obtaining an attractive combination of high volumetric capacity and rate capability, using a cheap, scalable and practical processing technique. TiO_2 is chosen as the demonstrator material for this study, because it is readily available in different morphologies, and the electrode structuring principles described are essentially materials-independent.

Two types of TiO_2 were selected: laboratory synthesized porous TiO_2 particles (P-TiO_2, $\sim$200 nm) with $\sim$40 nm diameter internal pores tunnelling through the particles, and commercial non-porous TiO_2 nanoparticles (N-TiO_2, $\sim$25 nm). The two layer electrode design rationale was as follows and is shown schematically in Figure 1(a). First we placed P-TiO_2 immediately adjacent to the current collector, furthest away from the separator, with the intention to facilitate Li ion transport through the P-TiO_2

internal pores in the region of the electrode where Li ion transport is often restricted. However, if the entire electrode were made of P-TiO_2 only, volumetric capacity will be reduced because of the relatively high embodied pore volume (as shown later). Therefore, we decided that only half of the total electrode thickness should comprise P-TiO_2. Second, the other half of the electrode, adjacent to the separator, comprised smaller N-TiO_2. In this case, if the entire electrode were made of N-TiO_2 only, volumetric capacity might be increased but ion mobility may become restricted in the electrode region nearer to the current collector so that capacity faded more rapidly as C rate increased (as shown later). In summary, our approach investigates if a P-TiO_2 layer combined with an N-TiO_2 layer can exploit the positive aspects of both TiO_2 morphologies more effectively than electrodes made of either material alone or a blended random mixture of the two types of TiO_2. We also use spatially resolved, direct Li ion concentration measurements to understand how electrochemical performance improvements relate to electrode structure.

Figure 1(b) is a cross-sectional scanning electron microscopy (SEM) image of the two layer electrode after pressing. The total electrode thickness was 12.2 μm, excluding the thickness of current collector, extending beyond the field of view. The magnified cross-sectional SEM image of the P-TiO_2-based layer (next to the current collector) showed a relatively porous structure, while the magnified cross-sectional SEM image of the N-TiO_2-based layer (next to the separator) showed a denser structure, as intended. Figures S1(a)-(c) in the supplementary information (SI) show cross-sectional SEM images of the N-TiO_2-based electrode ([N]), P-TiO_2-based electrode ([P]) and an electrode based on random blend of N-TiO_2 and P-TiO_2 ([B]), where the total amount of TiO_2 was kept the same in all electrodes. Figures S1(a)-(b) show the microstructure of [N] and [P] electrodes was consistent with the [N] and [P] sub-layers in the [2L] electrode in Figure 1(b), while Figure S1(c) shows that the [B] electrode exhibited a more irregular microstructure due to the random mix of N-TiO_2 and P-TiO_2.

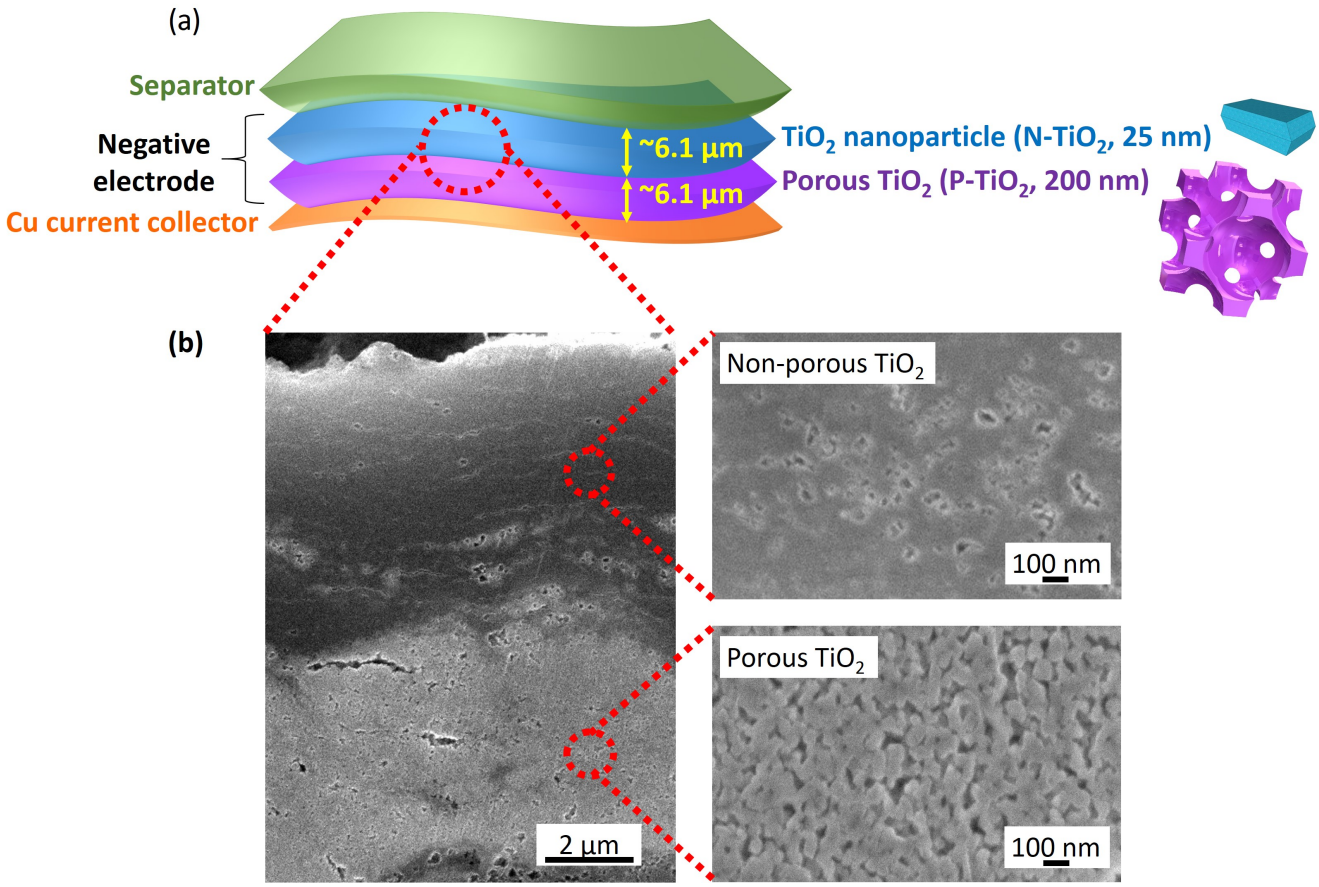

Figure 1: (a) Schematic diagram of a two layer electrode structure comprising different TiO_2 morphologies in each layer; and (b) cross-sectional SEM image of the two layer electrode, with higher magnification cross-sectional SEM images of the individual layers.

2 Experimental section

2.1 Materials

To synthesize porous TiO_2 single crystals, 20 mmol L^{-1} TiF_4 was dissolved in 400 mmol L^{-1} water to which 180 mmol L^{-1} 1-methylimidazolium tetrafluoroborate was added. Silica templates (650 mg)

were added to 50 ml of the TiF_4 solution. A transparent mixture was formed and kept at 120 ^{o}C for 20 hr in an oven. Precipitates (TiO_2 particles with the silica templates) were formed at the bottom of the Teflon reactor, collected and the silica template was then selectively etched in 2 mol L^{-1} aqueous NaOH at 80 ^{o}C for 60 min in a polypropylene beaker. The porous TiO_2 particles were collected by centrifugation (3,000 rpm for 60 min) and washed several times in water and ethanol. Commercial TiO_2 nanoparticles were obtained from Sigma-Aldrich, UK. Commercial multi-wall carbon nanotubes (MWNTs) were obtained from Thomas Swan Advanced Materials, UK.

2.2 Electrode processing

The two layer electrode was made by a scalable suspension atomization and automatic spray deposition processing technique developed in our group [25, 26], as shown in Figures. 2(a) and (b). Two types of aqueous suspension were prepared through sonication: (1) a mixture of P-TiO_2, conductivity enhancer MWNTs and binder carboxymethyl cellulose (CMC); and (2) a mixture of N-TiO_2, MWNTs and CMC, both in the mass ratio 8:1:1. The MWNTs were used as an electrical conductivity enhancer and the CMC was used as a binder. The suspensions were pumped into separate nozzles, atomized into micro-droplets by compressed air, and consecutively sprayed to form two layers of the negative electrode on a Cu foil current collector maintained at 100 ^{o}C on a heated vacuum stage-chuck. Any fugitive water in the spray suspensions evaporated continuously on the heated stage as the electrodes formed. The nozzles moved in a pre-programmed zig-zag pattern along X and Y directions at 20 mm s^{-1} to spray an area up to 20 cm x 20 cm. The spray processing was performed in a cross flow of air, the restrictions and costs of conventional organic solvents (e.g. N-methylpyrrolidone) [27] were avoided by using aqueous suspensions only. The spray processing route had a production rate of $\sim$7 μm cm^{-2}

min^{-1}, and is scalable and capable of making 200 nm - 110 μm thick and up to 1 m x 20 cm large area electrodes with controlled electrode nanostructure using a drum coater variant [25]. Figure 2(c) shows a sprayed two layer electrode of 11 x 9 cm.

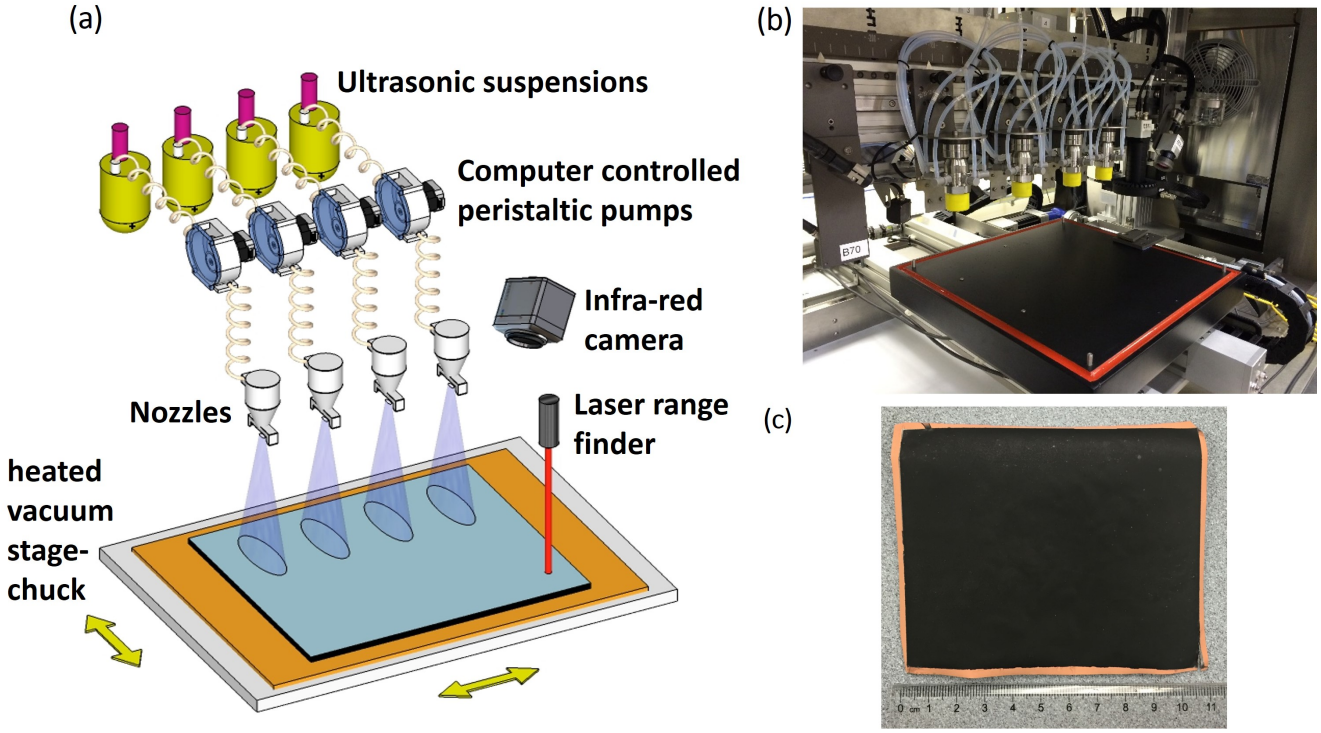

Figure 2: (a) Schematic diagram and (b) photo of the suspension atomization and automatic spray deposition equipment (Reprinted with permission from [26]. Copyright 2016 American Chemical Society); and (c) photo of a sprayed 11 x 9 cm two layer electrode showing scalability of the processing method.

To investigate energy storage benefits of layering the electrode structure, four types of negative electrode were made: (1) P-TiO_2 + MWNT ([P]), (2) N-TiO_2 + MWNT ([N]), (3) two layer electrode comprising of [P] and [N] sub-layers ([2L]) and (4) a conventional, blended random mix of the N-TiO_2, P-TiO_2 and MWNT ([B]). The [B] electrode had identical material fractions as the [2L] electrode and

differed only in that there was no sub-layer structure. The mass loading in each of the four types of negative electrode was kept the same at 2.9 mg $cm^{-2} \pm 4.8\%$ over 50 samples for comparison purposes, the mass loading was similar to other TiO_2 nanomaterial-based electrodes in the literature [28]. To compare volumetric capacities among the different structured electrodes, for the same mass loading but different electrode structures with different intrinsic porosities, the electrode thicknesses were 22.5, 8.4, 12.2 and 13.3 μm and the electrode loading densities were 1.3, 3.5, 2.4 and 2.2 g cm^{-3} for the [P], [N], [2L] and [B] electrodes respectively.

2.3 Cells

CR2032 coin half cells (1.13 cm^2 with a 1.2 cm diameter) were assembled in an Ar-filled glove box ($H_2O < 0.1$ ppm, $O_2 < 0.1$ ppm), using a glass fibre separator soaked with LP40 electrolyte (1 M $LiPF_6$ dissolved in ethylene carbonate (EC) and dimethyl carbonate (DMC, 1:1 v/v.)), and a metallic Li foil as the counter electrode.

2.4 Characterization

The electrode weight was measured by a microbalance (Sartorius) with 0.01 mg accuracy. The electrode thickness was measured by a Dektak 6M stylus profilometer (Veeco Instruments). The electrode active materials were investigated by X-ray diffraction (XRD, Siemens D5000) with a Cu_α radiation λ=1.5 $\mathring{A}$. The surface morphology of the electrodes was examined by SEM (JEOL 6500F). Cross section of the electrodes was prepared by a Gatan Precision Etching Coating System (PECS 685) at 6 kV beam for 1 hr. Post-mortem SEM images were obtained by opening coin cells after charge-discharge cycling in

an Ar-filled glove box to retrieve the negative electrodes, followed by washing in DMC several times. The electrode materials were also examined by high resolution transmission electron microscopy (TEM JEOL 2100F). The porosity and total pore area of the sprayed layers were evaluated through mercury porosimetry (Micromeritics AutoPore IV) operating at a pressure of 3.5 to 2 x 10^5 kPa.

Coin half cells were galvanostatically discharged (lithiation) and charged (delithiation) in the voltage range of 1.5 V to 3 V vs. Li/Li^+ at different charge/discharge rates at room temperature using a battery cycler (Arbin BT-G-25). X-ray photoelectron spectroscopy (XPS) was performed in an ion pumped Thermo Scientific K-Alpha 128-channel detecting analyzer equipped with an Al Kα X-ray source. The X-ray beam irradiated the surface of the sample and provided an X-ray spot size of 800 x 800 μm. Wide scans of the surface of the sample before and after depth profiling were performed at 100 eV. XPS depth profile measurements were performed using Ar^+ sputtering at 1000 eV and a beam raster of 2 x 2 mm^2 over the probe area. Detailed scans (20 eV) were performed on the surface of lithiated negative electrode, which were obtained from discharging (lithiating) coin half cells to 1.5 V and then opening the coin cells in an Ar-filled glove box to retrieve the negative electrodes, followed by washing in DMC several times. XPS depth profile measurements were collected every 25 s of sputtering time. At each etch level, detailed scans were collected at three different points on the sample to obtain representative data. The quantification of the fitted peaks was carried out using Avantage Version V5.952 software. Prior to peak fitting, the background contributions were subtracted using a Shirley function.

2.5 Performance calculation

Electrode loading density ρ (g cm^{-3}) was estimated by:

$$\rho = \frac{m}{A \times t} \tag{1}$$

where m was the mass of the electrode active materials (g), A was the area of the electrode (cm^2) and t was the thickness of the electrode (cm). Volumetric capacity C_{vol} (mAh cm^{-3}) was estimated by:

$$C_{vol} = \frac{C}{A \times t} \tag{2}$$

where C was the total capacity of the electrode (mAh). Gravimetric capacity C_{gra} (mAh g^{-1}) was estimated by:

$$C_{gra} = \frac{C}{m} \tag{3}$$

Coulombic efficiency η for the negative electrodes was calculated by:

$$\eta = \frac{C_{extraction}}{C_{intercalation}} \tag{4}$$

where $C_{intercalation}$ was the capacity during the discharge cycle and $C_{extraction}$ was the capacity during the charge cycle for negative electrodes.

3 Results and discussion

3.1 Materials and electrode structure

Figure 3(a) is a top-view SEM image of the as-sprayed [P] electrode. The P-TiO_2 particles were 180-220 nm, with 30-50 nm diameter internal pores spanning the particle internal diameter to facilitate ion transport. The MWNTs were 12-18 nm in diameter and 800 nm - 1 μm in length, forming a percolating

network for high electrical conduction throughout the electrode. Figure 3(b) is a TEM image showing a single P-TiO_2 particle. The light circles in the particle indicate the pores in the particle where electrons passed through under TEM. Figure 3(c) shows the crystal lattice planes of P-TiO_2 with a (101) *d*-spacing of 0.36 nm conforming to crystalline anatase. Figure S2 in the Supplementary Information (SI) is an XRD pattern of the pristine P-TiO_2 particles. The well-defined peaks also confirmed that the P-TiO_2 was crystalline anatase [18].

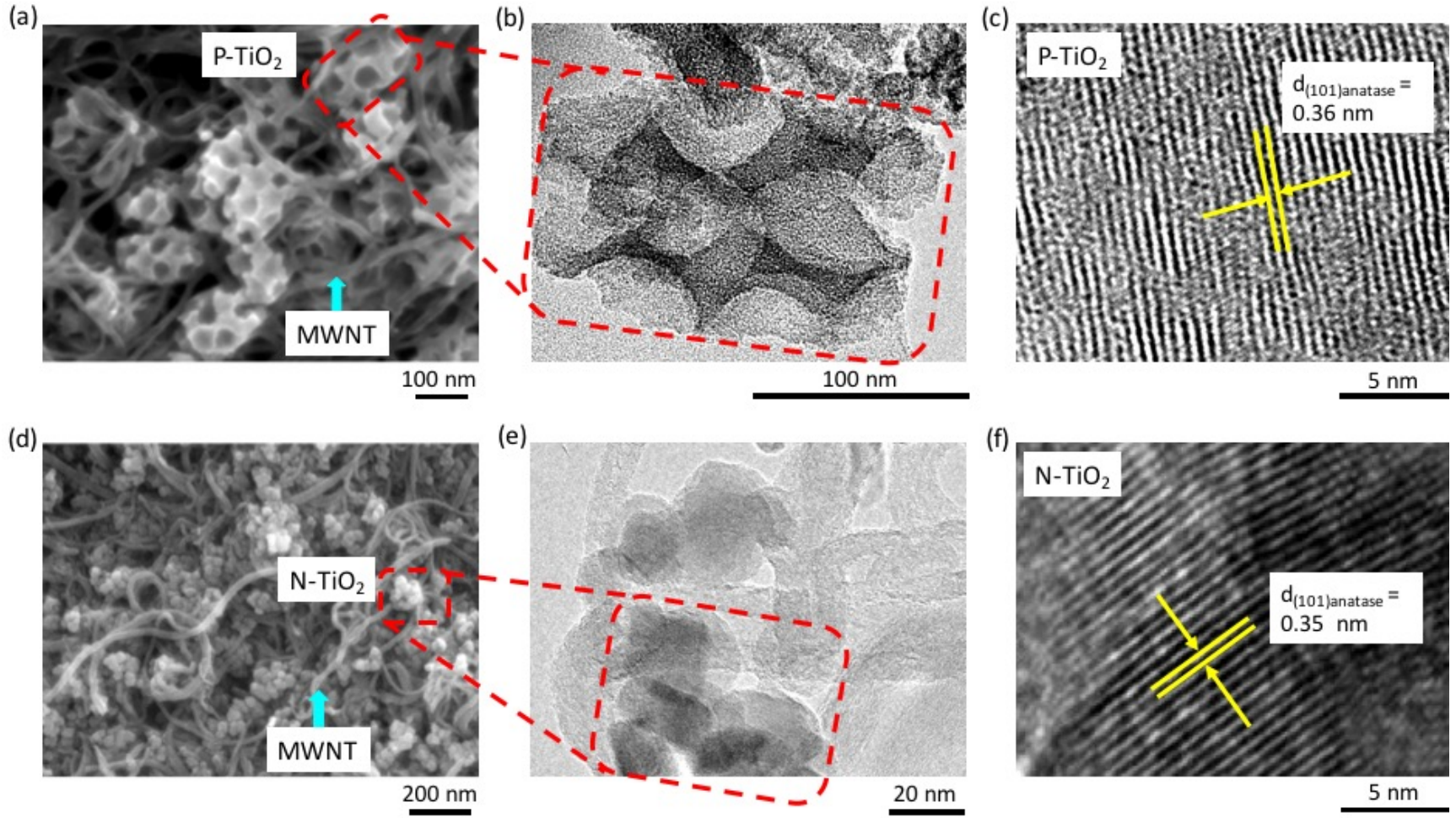

Figure 3: Top-view SEM images of as-sprayed (a) [P] and (d) [N] electrodes; TEM images of (b) laboratory synthesized porous P-TiO_2 particle and (e) commercial non-porous N-TiO_2 nanoparticles; high resolution TEM images showing crystal lattice planes of (c) P-TiO_2 and (f) N-TiO_2.

Figure 3(d) is a top-view SEM image of the as-sprayed [N] electrode with 20-30 nm N-TiO_2 nanoparticles and the same interconnected MWNT network that facilitated the electrical conductivity of the electrode. Figure 3(e) is a TEM image of the N-TiO_2 nanoparticles intertwined by the MWNTs. Figure 3(f) shows the crystal lattice planes of the N-TiO_2 nanoparticle with a (101) *d*-spacing of 0.35 nm, again conforming to crystalline anatase.

The porosity of the *as-sprayed* [P] and [N] electrodes was quantified by mercury porosimetry measurements, which are usually performed on powders [29], whereas here the porosity of the *sprayed electrodes* on a Cu foil themselves was measured. Before the measurement, a control test was performed first to confirm that the Cu foil did not contribute to the measurement of porosity [26]. During the measurement, hydrostatic pressure was increased progressively to infiltrate mercury from the upper, free surface of the electrode into the pores towards the underlying current collector. The measured total pore area and porosity for the [P] electrode were 169 m^2g^{-1} and 40.7% respectively, higher than 94 m^2g^{-1} and 22.6% for the [N] electrode, due to the inherent porous structure of the P-TiO_2 particles.

3.2 Electrochemical characterization

CR2032 coin half-cells were assembled using a metallic Li foil as the counter electrode and LP40 as the electrolyte to investigate electrochemical performance of the differently structured negative electrodes. Figures 4(a)-(d) show the galvanostatic discharge (Li intercalation) and charge (Li extraction) profiles of the [N], [P], [2L] and [B] negative electrodes in the second cycle at 0.1 C (1 C = 335 mA g^{-1}), showing both volumetric and gravimetric capacities. Figures S3(a)-(d) show the discharge and charge profiles of the four types of electrode in the first cycle with curve shapes and the trend in relative consistent

capacities with Figures 4(a)-(d). The potential plateaux in the discharge and charge processes were due to Li intercalation into and extraction from the interstitial octahedral sites of anatase TiO_2 according to [30–32]:

$$TiO_2 + xLi^+ + xe^- \leftrightarrow Li_xTiO_2 \tag{5}$$

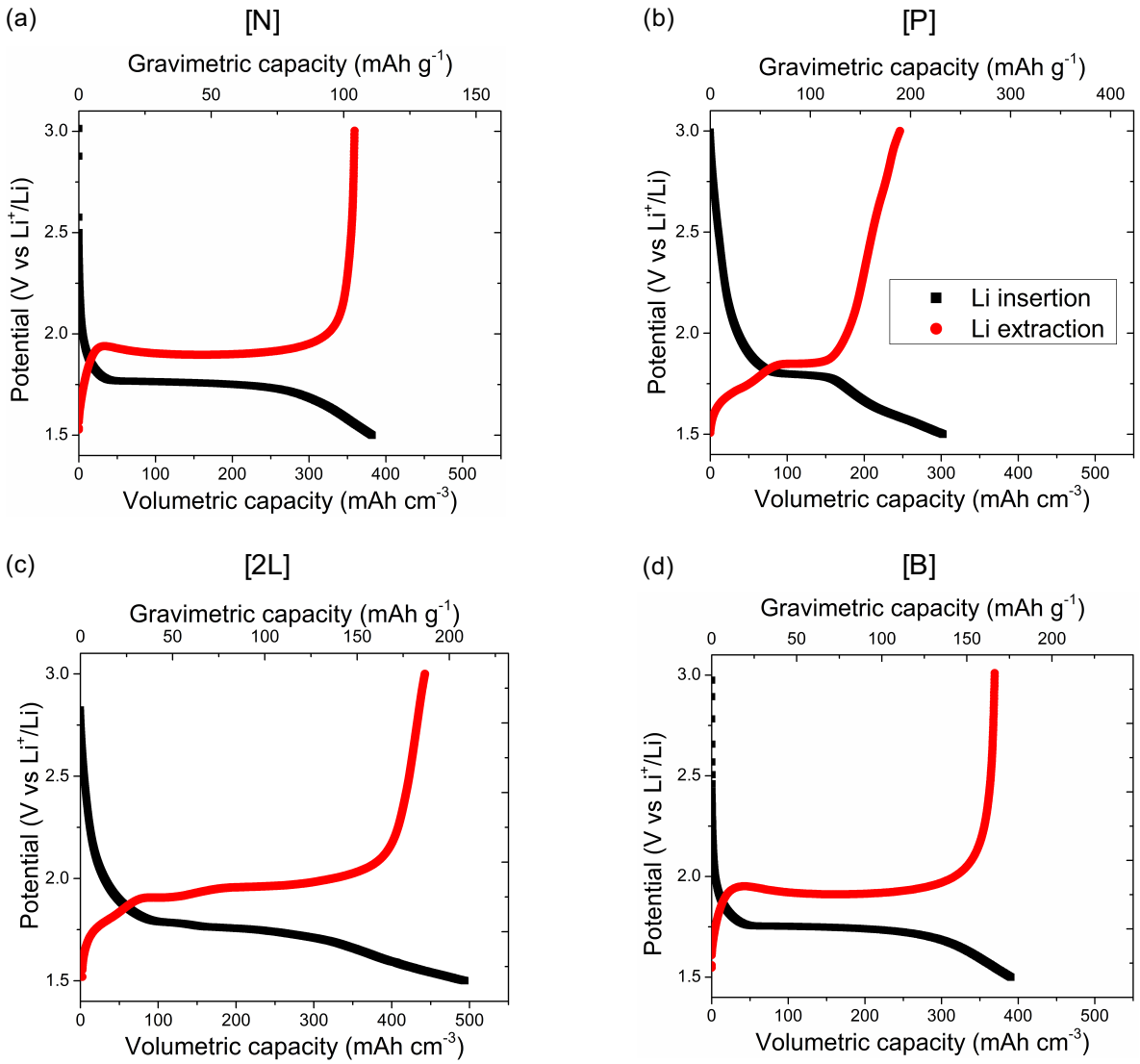

Figure 4: Galvanostatic discharge (Li intercalation) and charge (Li extraction) profiles for (a) [N], (b) [P], (c) [2L] and (d) [B] negative electrodes in the second cycle at 0.1 C.

Complete reduction of Ti^{4+} to Ti^{3+} during Li intercalation (ratio of Li per TiO_2, $x_{Li+} = 1$) would correspond to a theoretical capacity of 335 mAh g^{-1} [33–35], although most reports of Li intercalation/extraction in anatase TiO_2 particles larger than 10 nm give $x_{Li+} \approx 0.5$ at room temperature, corresponding to a capacity of ~170 mAh g^{-1} because the theoretical capacity of anatase TiO_2 can only be reached in the first 4 nm of the particles due to poor ionic conductivity of Li_1TiO_2 phase nucleated at the surface [32, 34–36].

Figure 4(b) shows that the [P] electrode exhibited shorter plateaux, but more sloped potential changes at the intercalation and extraction curves respectively than those of the [N] electrode in Figure 4(a), indicating that more charge was stored in the near-surface regions of the porous TiO_2 particles [37]. Although the [B] electrode contained the same materials as the [2L] electrode, the intercalation and extraction profiles of the [B] electrode were more similar to those of [N] electrode without the sloped potential changes, indicating that the large surface area of the P-TiO_2 particles was not efficiently used in the randomly blended [B] electrode structure.

Figures 4(a)-(d) show that volumetric capacities varied among the four types of electrode at a slow 0.1 C charge/discharge rate. The [N] electrode exhibited a high reversible volumetric capacity of 359.1 mAh cm^{-3} compared with 246.3 mAh cm^{-3} for the [P] electrode due to the smaller nanoparticle diameter (20-30 nm) and higher electrode loading density in the [N] electrode, but a lower gravimetric capacity of 104.7 mAh g^{-1} compared with 189.2 mAh g^{-1} for the [P] electrode due to more restricted Li ion diffusion in the [N] electrode, and hence lower active nanomaterial utilization in the electrode region near to the current collector. The [P] electrode had a higher gravimetric capacity than the [N] electrode because Li ions were able to travel to all regions in the electrode aided by the internal pores of the P-TiO_2 particles. As shown later, this effect becomes more pronounced at faster charge-discharge rates.

Although the [B] electrode balanced the volumetric and gravimetric capacities at 0.1 C (369.3 mAh cm^{-3} and 166.2 mAh g^{-1} respectively), the [2L] electrode had the highest reversible volumetric capacity of 442.6 mAh cm^{-3} (186.8 mAh g^{-1}) among the four types of electrode, because in the [B] electrode, the smaller N-TiO_2 nanoparticles may have blocked some of the pores in the larger P-TiO_2 particles (N-TiO_2 $\sim$25 nm and P-TiO_2 pores $\sim$40 nm), reducing active material utilization [38]. This negative synergistic interaction between the two types of TiO_2 were avoided in the discrete layered electrode structure. Thus, the deliberate layering of active nanomaterials, arranging and utilizing them more rationally in the [2L] electrode structure, was shown to enable high volumetric capacities.

The coulombic efficiency (capacity of Li extraction / capacity of Li intercalation) as a function of cycle number up to 100 cycles for the four types of electrode are shown in Figures S4-7 in the SI. The coulombic efficiencies for the [N], [P], [2L] and [B] electrodes during the first cycle were 86%, 78%, 83% and 85% and similar to data [39] in the literature. The lower initial coulombic efficiency for the [P] electrode was due to Li ions inserting into irreversible sites of the more porous, higher surface area P-TiO_2 particles during the first few cycles [40], where the number of surface defects and vacancies was expected to be comparatively high for the high surface area material [41]. Figures S4-7 in the SI also show that the coulombic efficiencies increased after the first cycle for all of the electrodes. The coulombic efficiency of the [P] electrode stabilized at 95% at the 18th cycle. The coulombic efficiency of the [2L] electrode stabilized at 95% much faster, at the 5th cycle, and was 99% over 100 cycles, suggesting a reduced number of irreversible reactions when the P-TiO_2 fraction was reduced and placed furthest from the separator.

To investigate the relationship between rate capability and electrode structure, Figure 5(a) shows the Li

extraction profiles of the [N], [P], [2L] and [B] negative electrodes at a faster 2 C charge/discharge rate. The [N] electrode had a lower volumetric capacity (36.1 mAh cm^{-3}) than the [P] electrode (98.1 mAh cm^{-3}) because the internal porosity of the P-TiO_2 particles facilitated faster ion diffusion, as previously described. Sensibly, the [B] electrode had a capacity between those of the [N] and [P] electrodes (85.7 mAh cm^{-3}) since it contained a blended mixture of both P-TiO_2 and N-TiO_2. Again, the [2L] electrode had the highest volumetric capacity of 147.5 mAh cm^{-3}, consistent with the hypothesis that layering should improve volumetric capacity over the [P] electrode, and improve Li ion diffusion in the otherwise denser electrode regions of the [N] and [B] electrodes. The reversible gravimetric capacity of the [2L] electrode was 64.6 mAh g^{-1} when the charge-discharge rate was increased to 2 C, much higher than 36.1 mAh g^{-1} at the same rate for an anatase TiO_2-graphene aerogel 3D hybrid electrode with a similar electrode film thickness [42], showing higher rate performance of the [2L] electrode.

Since [2L] and [P] electrodes exhibited the highest volumetric capacities among the four types of electrode at 2 C in Figure 5(a), Figure 5(b) compares their reversible volumetric capacities (during Li extraction) over a range of C rates. Figures S8(a) and (b) in the SI show the corresponding detailed discharge and charge profiles. These data demonstrated that although the rate performance of both [P] and [2L] electrodes decreased with an increasing C rate, the [2L] electrode consistently had the higher volumetric capacity than the [P] electrode over the C rate range studied.

Figure S9 in the SI shows that the capacity retention of the [2L] electrode at 0.1 C was 94% after 100 cycles. This stability was much higher than 59% reported for an anatase TiO_2-graphene aerogel 3D hybrid electrode [42]. Figure S10 shows an SEM cross-sectional image of the [2L] electrode after charge-discharge cycling, showing excellent electrode stability to cycling [43]. While other layering configurations such as swapping the locations of P-TiO_2 and N-TiO_2 and/or changing the thickness ratio

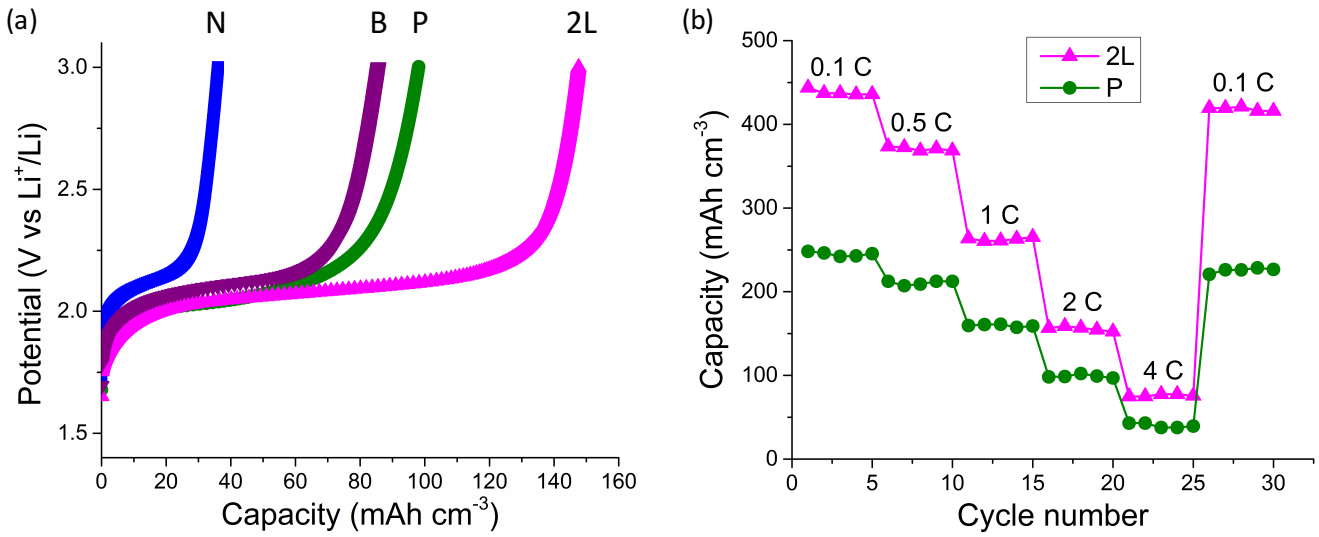

Figure 5: Galvanostatic charge (Li extraction) profiles for the negative electrodes of N-TiO_2 only ([N]), P-TiO_2 only ([P]), two layer ([2L]) and randomly blended ([B]) at 2 C; and (b) reversible volumetric capacities of [P] and [2L] electrodes over a range of C rates.

between the two layers, as well as making thicker electrodes up to 100 μm continue to be investigated, here, we show for the first time how layering of the electrode structure, using a scalable processing approach, can significantly improve the performance of electrodes, e.g. an increase in volumetric capacity of 72% over a randomly blended mixtures of the identical materials at 2C.

Figure S11 shows the Nyquist plots of the [N], [P] and [2L] electrodes, which were resolved to a semi-circle at high to intermediate frequency and a sloping line at low frequency. The intercept of the Nyquist plot with the Z' axis at high frequency was used to estimate the equivalent series resistance (ESR), which was mainly attributed to the resistance of the electrolyte and contact resistance between the electrode and current collector [44]. The ESR in Figure S11 was little changed at 6.7, 6.9 and 6.8 Ω for the [N], [P] and [2L] negative electrodes respectively. Since the three electrodes used the same electrolyte, the similar ESRs suggest the P-TiO_2 layer did not reduce the adhesion to the Cu current

collector, and wetting and adhesion of the electrodes to the Cu current collector were broadly similar among the electrodes.

3.3 Li concentration profile

To support the interpretation of electrode behavior in terms of Li ion concentration gradients through the electrode thickness, for the first time to the best of our knowledge, we present direct evidence of the effect of electrode structure on the Li ion spatial concentration. This was achieved using XPS depth profiling after the electrodes had completed one Li intercalation cycle.

During XPS depth profiling, Ar ions were used to sputter from the electrode surface (the region nearest to the separator) and into the electrode thickness at an etch speed of 1.1 nm s^{-1}, as shown schematically in Figure 6(a). The electrode surface chemical composition was analyzed every 25 s of the etching time. At each etch level, detailed scans of Li_{1s} and Ti_{2p} spectra were collected at three different positions on the sample to obtain representative data. An XPS peak-fitting methodology was applied consistently to all XPS spectra to ensure a robust peak intensity comparison. However, it proved impossible to depth profile through the 12.2 μm thick electrodes, and so thinner (780 nm) electrodes, but with otherwise identical electrode structure, were fabricated, so that depth profiling could be performed within a realistic time frame. For the thinner [2L] electrode, the N-TiO_2 layer (next to the separator) was $\sim$370 nm and the P-TiO_2 layer (next to the current collector) was $\sim$410 nm. Thinner [N] and [P] electrodes with similar mass loading as the thinner [2L] electrode were also fabricated for like-for-like comparison to understand how the [2L] electrode structure can improve Li ion diffusion dynamics. To compensate approximately for the effect of the thinner electrodes, and to emphasize any Li ion dynamics differences

between the electrodes, the discharge rate (Li intercalation) for the single cycle was increased to 13 C. Figure S12 shows the charge and discharge curves of the second cycle for the thinner [2L] electrode used in the XPS depth profiling measurements, showing performance consistency $\pm 6\%$ with the thicker electrodes in Figure 4(c). Figures S12-S14 are XPS wide scan spectra for the [N], [P] and [2L] electrodes showing the same element peaks before and after Ar ion sputtering, confirming electrode stability before and after depth profiling [5, 45].

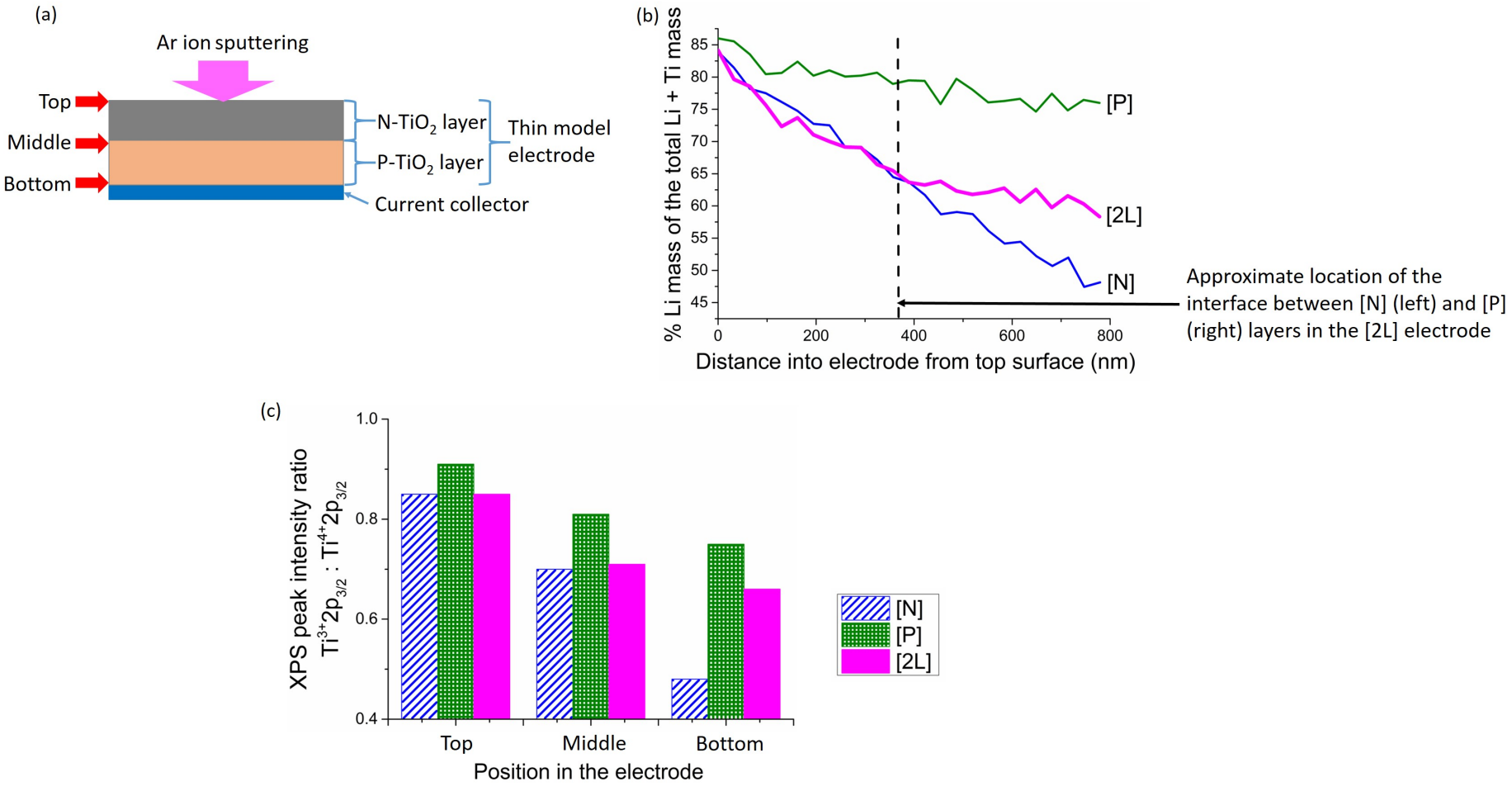

Figure 6: (a) A schematic diagram showing the geometry of how Ar ion sputtering XPS depth profiling was achieved using a thin two layer electrode model; (b) % Li mass of the total Li + Ti mass in the electrode as a function of distance into electrode from top surface for the [N], [P] and [2L] electrodes to show Li ion concentration through electrode thickness; and (c) XPS peak intensity ratio between $Ti^{3+}2p_{3/2}$ and $Ti^{4+}2p_{3/2}$ at different positions in the electrode to show Li intercalation into TiO_2 through electrode thickness.

Figure 6(b) shows the % Li mass to (Li+Ti) mass in the electrode as a function through thickness from the "top" position next to the separator to the "bottom" position next to the current collector, as shown schematically in Figure 6(a). For the [N] electrode, % Li reduced by 42% from "top" to "bottom" of the electrode. For the [P] electrode, % Li decreased much more slowly, by only 12% because of the higher intrinsic porosity and better ion diffusion through the electrode. For the [2L] electrode, % Li decreased at the same rate as the [N] electrode in the N-TiO_2 layer nearest to the separator, but then decreased more slowly and in a similar fashion to the [P] electrode in the P-TiO_2 layer nearest to the current collector. Figure 6(b) shows a gradual change in the slope of % Li mass to (Li+Ti) mass curve at the interface between the [N] and [P] layers, suggesting a gradual transition in the local Li ion diffusion coefficient at the interface. Figure 6(b) also shows that the relatively dense [N] layer did not cause a significant restriction on ion diffusion in this region, and Li ions were relatively abundant nearest to the separator, as has also been suggested by modelling [9].

Further, because Equation 4 shows that charge storage involves the reduction of Ti^{4+} to Ti^{3+}, the $Ti^{3+}2p_{3/2}/Ti^{4+}2p_{3/2}$ intensity ratio from the Ti_{2p} spectrum can provide a direct measurement of the TiO_2 fraction converted to Li_xTiO_2 and thus the extent of Li^+ intercalation into TiO_2. Detailed Ti_{2p} spectra for depth profiling of the three electrodes are shown in Figure S15(a)-(c). The $Ti^{3+}2p_{3/2}/Ti^{4+}2p_{3/2}$ intensity ratios for the top, middle and bottom regions of the [N], [P] and [2L] electrodes are summarized in Figure 6(c). For the [N] electrode, the $Ti^{3+}2p_{3/2}/Ti^{4+}2p_{3/2}$ intensity ratio decreased by 44% from the top to the bottom. For the [P] electrode, the $Ti^{3+}2p_{3/2}/Ti^{4+}2p_{3/2}$ intensity ratio decreased much less, by only 18%. For the [2L] electrode, the $Ti^{3+}2p_{3/2}/Ti^{4+}2p_{3/2}$ intensity ratio was similar to those of the [N] electrode in the N-TiO_2 layer (from the top to the middle), *but* much higher and more similar to the [P] electrode in the P-TiO_2 layer (from the middle to the bottom). This trend confirmed the hypothesis that layering could maintain higher TiO_2 utilization in this region

of the [2L] electrode. When the insights from the % Li plots in Figure 6(b) and the Li intercalation measurements in Figure 6(c) are combined with volumetric capacity measurements in Figure 5(a), it may be concluded that engineering the physical arrangement of the active nanomaterials in the electrode structure - with no change in the underlying electrochemical reactions - can increase the fraction of nanomaterial involved in energy storage reactions and improve the rate retention performance of a Li-ion battery negative electrode.

4 Conclusions

A two layer negative electrode for Li ion batteries has been manufactured in which two types of nanoscale TiO_2 with different morphologies were placed in discrete layers within the electrode to achieve a combination of high volumetric capacity and rate capability that was un-achievable by either material on its own, or by a blended mixture of the materials. Volumetric capacities were reported for the different electrode structures, each with the same carefully controlled mass fraction of active nanomaterials. Optimally, porous TiO_2 particles were located in a sub-layer of the electrode furthest from the separator Li concentrations were otherwise more limited, while smaller, better packed non-porous TiO_2 nanoparticles were located in the layer nearest to the separator where Li ion concentrations were relatively high and contributed to a high volumetric capacity. The structuring placed porous materials that promote ion mobility, but reduce volumetric capacity, only where they were most effective. A direct correlation between the local Li concentration and the extent of local Li intercalation through the thickness of the two layer electrode was revealed by XPS depth profiling. These data confirmed that the higher volumetric capacity of the two layer electrode at higher C rates was due to higher Li ion concentrations in regions of the electrode furthest from the separator. The optimized two layer electrode was demonstrated at an

area of 11 cm x 9 cm using a flexible suspension atomization and spray deposition technique. The work suggests that even relatively simple structuring of electrodes comprising different morphologies of nanomaterials, using processes that are scalable beyond the laboratory, can exploit the intrinsic advantages of each nanomaterial in order to make significant improvements to overall ion dynamics and capacity retention, without interfering with the underlying electrochemical reactions. Thus, better performance from existing, commercially accepted materials may be realizable simply by structuring their electrodes more rationally. Alternatively, this approach may also be suitable for introducing next generation energy storage materials progressively as discrete layers within electrode configurations.

Acknowledgments

This work was partly supported by the UK Engineering and Physical Sciences Research Council through Grant EP/M009521/1 - "Enabling Next Generation Li-ion Batteries". The author would like to thank Prof Peter G. Bruce, Dr Andy Naylor and Mr Niccolo Guerrini for the precision etching and coating system (PECS) sample preparation and mercury porosimetry measurements.

References

[1] S. Chae, M. Ko, S. Park, N. Kim, J. Ma, J. Cho, Micro-sized Fe-Cu-Si ternary composite anodes for high energy Li-ion batteries, Energy Environ. Sci., DOI: 10.1039/c6ee00023a (2016).

[2] B. Kang, G. Ceder, Battery materials for ultrafast charging and discharging, Nature, 458 (2009) 190-193.

[3] B. Dunn, H. Kamath, J.-M. Tarascon, Electrical energy storage for the grid: a battery of choices, Science, 334 (2011) 928-935.

[4] Y. Zhao, Y Ding, Y Li, L. Peng, H. R. Byon, J. B. Goodenough, G. Yu, A chemistry and material perspective on lithium redox flow batteries towards high-density electrical energy storage, Chem. Soc. Rev., 44 (2015) 7968-7996.

[5] S. Brutti, V. Gentili, H. Menard, B. Scrosati, P. G. Bruce, TiO_2-(B) nanotubes as anodes for lithium batteries: origin and mitigation of irreversible capacity, Adv. Energy Mater., 2 (2012) 322-327.

[6] T. F. Fuller, M. Doyle, J. Newman, Simulation and optimization of the dual lithium ion insertion cell, J. Electrochem. Soc., 141 (1994) 1-10.

[7] R. Gonzalez-Arrabal, M. Panizo-Laiz, K. Fujita, K. Mima, A. Yamazaki, T. Kamiya, Y. Orikasa, Y. Uchimoto, H. Sawada, C. Okuda, Y. Kato, J. M. Perlado, Meso-scale characterization of lithium distribution in lithium-ion batteries using ion beam analysis techniques, J. Power Sources, 299 (2015) 587-595.

[8] C. Han, D. Yang, Y. Yang, B. Jiang, Y. He, M. Wang, A.-Y. Song, Y.-B. He, B. Li, Z. Lin, Hollow titanium dioxide spheres as anode material for lithium ion battery with largely improved rate stability and cycle performance by suppressing the formation of solid electrolyte interface layer, J. Mater. Chem. A, 3 (2015) 13340-13349.

[9] M. Ebner, D.-W. Chung, R. E. Garcia, V. Wood, Tortuosity anisotropy in lithium-ion battery electrodes, Adv. Energy Mater., 4 (2014) 1301278 1-6.

[10] Y.-H. Chen, C.-W. Wang, X. Zhang, A. M. Sastry, Porous cathode optimization for lithium cells: ionic and electronic conductivity, capacity, and selection of materials, J. Power Sources, 195 (2010) 2851-2862.

[11] J. Zhu, T. Wang, F. Fan, L. Mei, B. Lu, Atomic-scale control of silicon expansion space as ultrastable battery anodes, ACS Nano, 10 (2016) 82438251.

[12] Y. Yang, B. Wang, J. Zhu, J. Ling, J. Zhu, R. Podila, A. M. Rao, B. Lu, Bingan, Bacteria absorption-based $Mn_2P_2O_7$-carbon@reduced graphene oxides for high-performance lithium-ion battery anodes, ACS Nano, 10 (2016) 5516-5524.

[13] S. Klink, W. Schuhmann, F. L. Mantia, Vertical distribution of overpotentials and irreversible charge losses in lithium ion battery electrodes, ChemSusChem, 7 (2014) 2159-2166.

[14] S.-H. Ng, F. L. Mantia, P. Novak, A multiple working electrode for electrocemical cells: a tool for current density distribution studies, Angew. Chem. Int. Ed., 48 (2009) 528-532.

[15] Z. Chen, I. Belharouak, Y.-K. Sun, K. Amine, Titanium-based anode materials for safe lithium-ion batteries, Adv. Funct. Mater., 23 (2013) 959-969.

[16] M. A. Khan, Y.-M. Kang, Synthesis and electrochemical analysis of a nanastructured spindle shaped TiO_2, Mater. Lett., 156 (2015) 209-213.

[17] J. M. Feckl, K. Fominykh, M. Doblinger, D. Fattakhova-Rohlfing, T. Bein, Nanoscale porous framework of lithium titanate for ultrafast lithium insertion, Angew. Chem. Int. Ed., 51 (2012) 7459-7463.

[18] Y. Ren, L. J. Hardwick, P. G. Bruce, Lithium intercalation into mesoporous anatase with an ordered 3D pore structure, Angew. Chem. Int. Ed., 49 (2010) 2570-2574.

[19] Y. Ren, Z. Liu, F. Pourpoint, A. R. Armstrong, C. P. Grey, P. G. Bruce, Nanoparticulate TiO_2(B): an anode for lithium-ion batteries, Angew. Chem. Int. Ed., 51 (2012) 2164-2167.

[20] E. Eustache, P. Tilmant, L. Morgenroth, P. Roussel, G. Patriarche, D. Troadec, N. Rolland, T. Brousse, C. Lethien, Silicon-microtube scaffold decorated with anatase TiO_2 as a negative electrode for a 3D lithium-ion microbattery, Adv. Energy Mater., 4 (2014) 1301612.

[21] Y. Chen, X. Ma, X. Cui, Z. Jiang, In situ synthesis of carbon incorporated TiO_2 with long-term performance as anode for lithium-ion batteries, J. Power Sources, 302 (2016) 233-239.

[22] J. Brumbarov, J. P. Vivek, S. Leonardi, C. Valero-Vidal, E. Portenkirchner, J. Kunze-Liebhauser, Oxygen deficient, carbon coated self-organized TiO_2 nanotubes as anode material for Li-ion intercalation, J. Mater. Chem. A, 3 (2015) 16469-16477.

[23] M. Wagemaker, F. M. Mulder, M. Fokko, Properties and promises of nanosized insertion materials for Li ion batteries, Acc. Chem. Res., 46 (2013) 1206-1215.

[24] Y. Gogotsi, P. Simon, True performance metrics in electrochemical energy storage, Science, 334 (2011) 917-918.

[25] X. Zhao, B. T. T. Chu, B. Ballesteros, W. Wang, C. Johnston, J. M. Sykes, P. S. Grant, Spray deposition of steam treated and functionalized single-walled and multi-walled carbon nanotube films for supercapacitors, Nanotechnology, 20 (2009) 065605.

[26] C. Huang, J. Zhang, H. J. Snaith, P. S. Grant, Engineering the membrane/electrode interface to improve the performance of solid-state supercapacitors. ACS Appl. Mater. Interfaces, 8 (2016) 20756-20765.

[27] D. L. Wood III, J. Li, C. Daniel, Prospects for reducing the processing cost of lithium ion batteries, J. Power Sources, 275 (2015) 234-242.

[28] M. Saito, Y. Nakano, M. Takagi, N. Honda, A. Tasaka, M. Inaba, Improvement of tap density of TiO_2(B) powder as high potential negative electrode for lithium ion batteries, J. Power Sources, 244 (2013) 50-55.

[29] Y. Zhao, J. Sun, X. Chen, H. Zhu, W. Yang, W. Synthesis and high-rate performance of spinel $Li_4Ti_5O_{12}$ with core-shell hierarchical macro-mesoporous structure. New J. Chem., 38 (2014) 1173-1178.

[30] M. Wagemaker, A. P. M. Kentgens, F. M. Mulder, Equilibrium lithium transport between nanocrystalline phase in intercalated TiO_2 anatase, Nature, 418 (2002) 397-399.

[31] X. Guan, J. Zheng, M. Zhao, L. Li, G. Li, Synthesis of $FeTiO_3$ nanosheets with 0001 facets exposed: enhanced electrochemical performance and catalytic activity, RSC Adv., 3 (2013) 13635-13641.

[32] Y. Tang, Y. Zhang, J. Deng, J. Wei, H. L. Tam, B. K. Chandran, Z. Dong, Z. Chen, X. Chen, Mechanical force-driven growth of elongated bending TiO_2-based nanotubular materials for ultrafast rechargeable lithium ion batteries, Adv. Mater., 26 (2014) 6111-6118.

[33] X. Zhang, H. Chen, Y. Xie, J. Guo, Ultralong life lithium-ion battery anode with superior high-rate capability and excellent cyclic stability from mesoporous Fe_2O_3@TiO_2 core-shell nanorods, J. Mater. Chem. A, 2 (2014) 3912-3918.

[34] W. J. H. Borghols, D. Lutzenkirchen-Hecht, U. Haake, E. van Eck, F. Mulder, M. Wagemaker, The electronic structure and ionic diffusion of nanoscale $LiTiO_2$ anatase, Phys. Chem. Chem. Phys., 11 (2009) 5742-5748.

[35] G. Wang, Z. Sun, F. Huang, C. Gong, H. Liu, G. Zheng, S. Wen, Carbon cloth supported anatase TiO_2 aligned arrays as a High-performance anode material for Li-ion batteries, Mater. Lett., 171 (2016) 150-153.

[36] E. Madej, S. Klink, W. Schuhmann, E. Ventosa, F. L. Mantia, Effect of the specific surface area on thermodynamic and kinetic properties of nanoparticle anatase TiO_2 in lithium-ion batteries. J. Power Sources, 297 (2015) 140-148.

[37] J. Wang, J. Polleux, J. Lim, B. Dunn, Pseudocapacitive contributions to electrochemical energy storage in TiO_2 (anatase) nanoparticles, J. Phys. Chem. C, 111 (2007) 14925-14931.

[38] C. Huang, J. Zhang, N. P. Young, H. J. Snaith, P. S. Grant, Solid-state supercapacitors with rationally designed heterogeneous electrodes fabricated by large area spray processing for wearable energy storage applications, Sci. Reports, 6:25684 (2016) DOI: 10.1038/srep25684.

[39] Y. Li, X. Hang, J. Liang, C. Lu, K. Ye, C. Hou, K. Yu, TiO_2 nanoflakes as anode material for lithium ion batteries, Synth. React. Inorg. M., 46 (2016) 1480-1484.

[40] X. Wang, Y. Wang, L. Yang, K. Wang, X. Lou, B. Cai, Template-free Synthesis of homogeneous yolk-shell TiO_2 hierarchical microspheres for high performance lithium ion batteries, J. Power Sources, 262 (2014) 72-78.

[41] Z. Y. Wang, X. W. Lou, TiO_2 Nanocages: Fast Synthesis, Interior Functionalization and Improved Lithium Storage Properties, Adv. Mater., 24 (2012) 41244129.

[42] J. Zhang, Y. Zhou, G. Zheng, Q. Huang, X. Zheng, P. Liu, J. Zhang, X. Guan, Novel assembly and electrochemical properties of anatase TiO_2-graphene aerogel 3D hybrids as lithium-ion battery anodes, Chem. Phys. Lett., 662 (2016) 214-220.

[43] J. Zhu, Z. Xu, B. Lu, Ultrafine Au nanoparticles decorated NiCo2O4 nanotubes as anode material for high-performance supercapacitor and lithium-ion battery applications, *Nano Energy*, 2014, **7,** 114-123.

[44] X. Li, D. Luo, X. Zhang and Z. Zhang, Enhancement of electrochemical pperformance for $LiFePO_4/C$ with 3D-grape-bunch structure and selection of suitable equivalent circuit for fitting EIS results, *J. Power Sources*, 2015, **291,** 75-84.

[45] J. Halim, K. M. Cook, M. Naguib, P. Eklund, Y. Gogotsi, J. Rosen, M. W. Barsoum, X-ray photoelectron spectroscopy of select multi-layered transition metal carbides (MXenes), Appl. Surf. Sci., 362 (2016) 406-417.

Vitae

Chun Huang received a B.Eng degree in Materials Science and Engineering from Imperial College London, UK in 2010 and a D.Phil degree in Materials from University of Oxford, UK in 2014. She is currently a Postdoctoral Researcher at University of Oxford. Her research interests are advanced materials and processing techniques for energy storage applications such as lithium ion batteries and supercapacitors.

Neil P. Young received his D.Phil degree from University of Birmingham, UK. He is currently a Senior

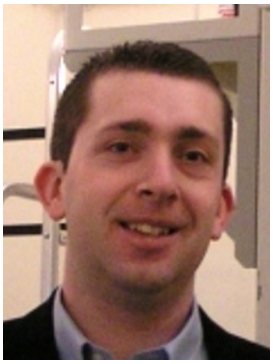

Research Fellow at Department of Materials, University of Oxford. He is focused on developing advanced TEM techniques such as HRTEM, STEM and electron exit-wave function restoration.

Jin Zhang received her D.Phil degree in Chemistry from University of Oxford, UK in 2005. She is currently a visiting researcher at University of Oxford. Her research field is synthesis development of new energy materials and new mesocrystal or nanocrystal materials.

Henry J. Snaith received his D.Phil degree from University of Cambridge, UK. He received a Junior

Research Fellowship for Clare College at University of Cambridge in 2006, and moved to the Department of Physics at University of Oxford in 2007. Following this, he was appointed a Research Councils UK Research Fellow then promoted to Reader and Professor. His research is focussed on developing new material structures for dye-sensitized and hybrid solar cells and understanding and controlling the physical processes occurring at interfaces. Professor Snaith became a Fellow of the Royal Society in 2015.

Patrick S. Grant received a B.Eng degree in Materials Engineering from the University of Nottingham, UK in 1987 and a D.Phil degree in Materials from the University of Oxford, UK in 1991. He has been Royal Society University Research Fellow, Reader and since 2004 the Vesuvius Professor of Materials in the Department of Materials with the University of Oxford. His research interests are the invention and use of novel processes to manufacture advanced materials for applications in structural, energy storage, and functional applications. Professor Grant became a Fellow of the Royal Academy of Engineering in 2008.